Bachelorarbeit am Fachbereich Physik

Characterization of a nanotip electron source for femtosecond point-projection microscopy

Jannik Malter

Matrikelnummer
4653340

09.05.2017

This work has been performed between November 2016 and May 2017 in the Max-Planck Research group 'Structural and electronic surface dynamics' headed by Dr. Ralph Ernstorfer, associated to the department of Physical Chemistry (headed by Prof. Dr. Martin Wolf) at the Fritz Haber Institute of the Max Planck Society.

Erstgutachter: Prof. Dr. Martin Wolf

Zweitgutachter: Prof. Dr. Jan Behrends

Contents

1 Introduction

To investigate the physical properties and ultrafast dynamics of nanometer scaled devices and materials, experimental probes which provide nanometer spatial- and femtosecond temporal resolution are required. Electrons with a kinetic energy below 1 keV are strongly sensitive to electric fields and have a de Broglie wavelength on the order of 1 Å, which allows for spatial resolution down to the sub-nm scale. Whereas ultrafast electron diffraction is a well-known tool to investigate the lattice structure of bulk materials in reciprocal space [1] [2], ultrafast imaging with low-energy electrons can be used to study nanoscale electric fields and photocurrents in real space. For this purpose, Müller et. al. developed a femtosecond point-projection electron microscope (fsPPM) [3] [4]. The principle of a PPM is simple: A point-like nanotip electron source emits a divergent electron beam which interacts with a sample. The apex of a nanotip has a radius of $\approx 25\,\mathrm{nm}$, which leads to a large local field enhancement. This confines electron emission to a very small space, which is ideal for a point-like source. To achieve femtosecond temporal resolution, the pump-probe technique is applied. The electron source is triggered with an ultrashort laser pulse, resulting in the emission of an ulrashort electron probe pulse.

Several challenges arise from the usage of ultrashort electron pulses: In contrast to ultrashort light pulses, electron pulses disperse in vacuum. First, electrons with different energies have different velocities and need a different amount of time to travel the same distance, which reduces the temporal resolution of the microscope. Because point-projection microscopy with low energy electrons is a lens-less design, tip-sample distances of only a few microns are achievable, reducing the impact of this effect.
Second, electrons are charged particles and interact with each other. During propagation through vacuum, a compact electron cloud expands due to repelling Coulomb forces, broadening the electron pulse in the spacial and temporal domain. This effect is called space charge and can be overcome by operating the electron source in the single-electron regime, which produces electron pulses consisting of only one electron.

For the operation of a fsPPM, the repetition rate of the laser system is an important parameter. For the pump-probe technique to work, the time between two laser pulses needs to be longer than the relaxation time of the reversible process under investigation, hence a low repetition rate is advantageous. At the same time, a high tip current is desired for the best signal-to-noise ratio. This can either be achieved by a high repeti-

tion rate, or a high pulse energy. While the tip current is limited by thermal instability at fast laser systems like 80 MHz oscillators, space charge effects constrain the use of few-kHz amplified laser systems with high pulse energies.

In this thesis, ultrafast electron emission from a gold nanotip at the transition through the single-electron regime is investigated at repetition rates between 200 kHz and 1 MHz. Emission processes are identified, the impact of space charge on the spatial resolution of the microscope is measured, and maximum image intensity is compared between multiple laser repetition rates.

2 Theoretical background

This chapter introduces the theoretical background of photoemission from laser triggered nanotip electron emitters. The first section describes the electron emission processes from metals in general, while the second section outlines the special characteristics of the nanotip geometry.

2.1 Electron emission from metals

In general, electron emission means extraction of electrons from matter into the vacuum. In a metal, the valence electrons can be described as a free electron gas, trapped inside a potential well. Electron emission can occur by excitation above the vacuum barrier or by tunneling through the vacuum barrier. Tunneling requires an energy state with equal potential behind the vacuum barrier, created by an electric field.

The average number of electrons populating an energy state E_i inside a metal is given by the Fermi-Dirac distribution

$$\bar{n}_i = \frac{1}{e^{(E_i - E_F)/k_B T} + 1} \tag{1}$$

with the Fermi energy E_F, the absolute temperature T and the Boltzmann constant k_B. The difference between the Fermi energy and the vacuum potential is called the work function Φ. It is characteristic for every material, with typical values between 2 eV and 5 eV [5]. It is also dependent on the surface and electric fields altering the height of the vacuum barrier, in which case the effective work function Φ^* is used, considering all influences. At a temperature of $T = 0\,\mathrm{K}$, every state up to the Fermi energy is populated, but none above. At a temperature of $T > 0\,\mathrm{K}$, electrons below the Fermi level start to populate higher energy states. Figure 2.1 shows the Fermi-Dirac distribution at $T = 0\,\mathrm{K}$ and $T = 1200\,\mathrm{K}$.

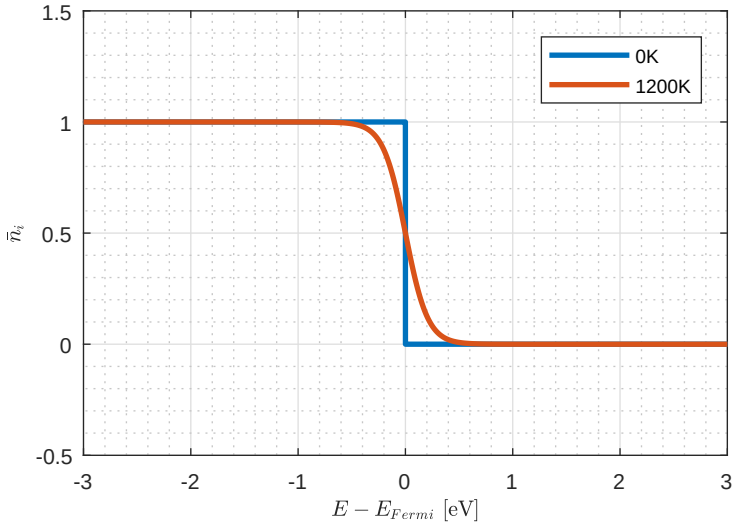

Figure 2.1: Fermi-Dirac distribution at 0 K (blue) and 1200 K (red). At temperatures $T > 0\,\mathrm{K}$ electrons from energy states below the Fermi level populate energy states above the Fermi level.

2.1.1 Static electron emission

Thermionic emission is the emission of electrons at high material temperatures due to the increasing population of energy states above the vacuum barrier. For significant thermionic emission, high temperatures of $T > 1000\,\mathrm{K}$ are required.

If an external electric field E_{dc} is applied, the width and height of the vacuum barrier decreases. This is called the Schottky Effect. Equation (2) describes the lowering of the work function as a function of E_{dc} with electron charge e and the vacuum permittivity ε_0.

$$\Delta W = \sqrt{\frac{e^3 E_{dc}}{4\pi\varepsilon_0}} \qquad W^* = W - \Delta W. \tag{2}$$

At low electric fields, where the width of the barrier is still so large that tunneling is negligible, the effect only enhances thermionic emission. Therefore, this regime is named field enhanced thermionic emission. At high electric fields of several volts per nanometer, where the width of the barrier is of the order of the electron wavelengths, tunneling becomes significant and electrons are emitted, even at a temperature of $T = 0\,\mathrm{K}$. This effect is called cold field emission or CFE.

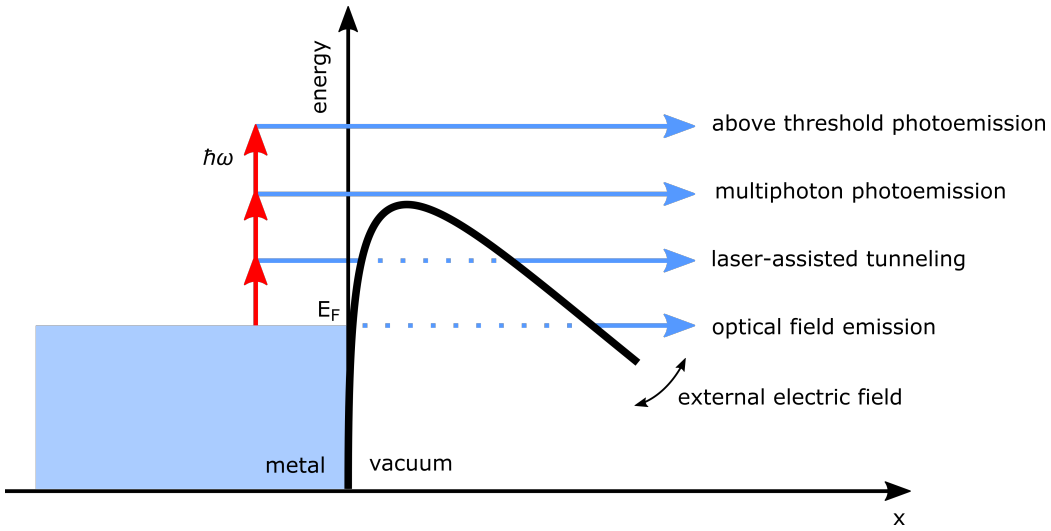

Figure 2.2: Different principles of electron emission. To be emitted, electrons have to overcome, or tunnel through, the vacuum-barrier. In case of multiphoton emission, the electrons absorb as many photons as needed to exceed the work function. The absorption of more photons than necessary is called above threshold photoemission. An external electric field, which can be static or originate from incident light, bends and lowers the vacuum barrier due to the Schottky effect. If its width is sufficiently small, electrons tunnel through it. In case of a DC field this is called cold field emission, in case of light strong-field emission.

2.1.2 Photoemission

Another mechanism for electron emission is the interaction with photons. An electron can absorb one or multiple photons to get excited into a higher energy state. The photons transfer their energy $E_{photons} = n \cdot \hbar\omega$ to the electron, with n being the number of photons absorbed, $\hbar$ the reduced Planck constant and ω the frequency of the photons. If the energy of one photon ($n = 1$) is larger than the work function, single-photon photoemission occurs. For $\hbar\omega < \Phi$, $n > 1$ photons are required. This is called multiphoton photoemission. The probability of absorbing multiple photons decreases with the number of photons. The emission current J_n, originating from an n-photon emission process, is proportional to the nth power of the light intensity I:

$$J_n \propto I^n \tag{3}$$

Hence, multiphoton photoemission becomes important when ultrashort laser pulses with high peak intensities are employed. The total emitted current is the sum of all contribut-

ing nth order processes, which is proportional to an effective nonlinearity n^*:

$$J = \sum_n J_n \qquad J \propto I^{n^*} \tag{4}$$

An electron can absorb more electrons than necessary to overcome the vacuum barrier. This process is called above threshold photoemission (ATP).

2.1.3 Optical field emission

The laser field is an alternating external electromagnetic field, periodically increasing and lowering the vacuum potential. At very intense light fields, the lowering is strong enough to allow for significant electron tunneling, called optical field emission [6]. It can be seen as cold field emission caused by the incident laser field. A lightfield with a wavelength of 750 nm has an optical period of 2.5 fs, resulting in tunneling windows below 1 fs [7]. The Keldysh parameter [8]

$$\gamma_k = \sqrt{\frac{\Phi}{2U_P}} \tag{5}$$

is used to differentiate between emission regimes, where U_P is the ponderomotive potential of the driving laser field given by

$$U_P = \frac{e^2 E_l^2}{4 m_e \omega^2}, \tag{6}$$

with the field amplitude E_l, frequency ω and the electron mass m_e. For $\gamma_k \gg 1$, the photon energy is large compared to the kinetic energy the electron gains from acceleration in the laser field. In this weak-field regime, the light field is treated as a perturbation and the emission process is described by multiphoton photoemission. For $\gamma_k \ll 1$, the laser field becomes strong enough to accelerate the electron to kinetic energies comparable to or larger than the electrons binding energy. In this strong field regime, the emission process is better described by laser field induced tunneling.

2.2 Metal nanotips as ultrafast electron emitters

When a metal with a highly curved surface feature is placed in an electric field, charges accumulate in that feature, causing an enhancement of the field. This affects static fields as induced by a bias voltage applied to the metal, as well as oscillating fields like an incident laser pulse.

The ratio between the electric field at this feature E_s and the electric field at a flat surface E_0 is called the field enhancement factor β

$$\beta = \frac{E_s}{E_0}. \tag{7}$$

For gold nanotips, field enhancement factors between 3 and 50 are reported and depend on the opening angle of the tip and the apex radius. The maximum field strength at the apex E_{max} can be approximated by

$$E_{max} = \frac{U}{\kappa R} \tag{8}$$

with the bias voltage U and the apex radius R. In reality, the apex is not a perfect sphere and κ describes the reduction of the field due to a deviation from it. In literature, $\kappa \approx 5$ is often used for typical field emission tips [9].

The strong field enhancement, combined with the nonlinearity of multiphoton photoemission, leads to an extreme localization of electron emission, which suits metal nanotips perfectly for electron point sources.

2.3 Electron pulse propagation in vacuum

Ultrashort electron pulses disperse while propagating through vacuum, which has to be taken into account for the operation of an ultrafast electron point-projection microscope. Therefore, several effects have to be considered.
Photoemitted electrons from a metal are not monochromatic. Electrons with a different kinetic energy propagate at a different speed and need a different amount of times to travel the same distance. This leads to a broadening of the pulse in the direction of propagation and reduces the temporal resolution of the microscope. Paarmann et. al. [10] simulated electron propagation from nanotip emitters and concluded that this effect is small compared to time of flight differences induced by the path length differences in the divergent beam. Because low-energy point-projection microscopes do not require any electron optical elements between the nanotip source and the sample, propagation distances of only a few microns are achievable, minimizing the impact of both effects.
A more important effect is the so-called space charge effect. Electrons are charged particles and repel each other. The force F acting on two electrons can be described by the

Coulomb law

$$F = \frac{1}{4\pi\epsilon_0}\frac{2e}{r^2}, \tag{9}$$

with the vacuum permittivity ϵ_0, the elementary charge e and the distance between the electrons r. It is an inverse square dependence, so at small distances the force gets very large. An electron cloud emitted from a nanotip has a very high electron density, leading to large forces between the electrons and to a significant expansion of the cloud during propagation, as depicted in Figure 2.3. Space charge has a large impact on spatial and temporal resolution [11] but it can be avoided by the usage of single-electron pulses.

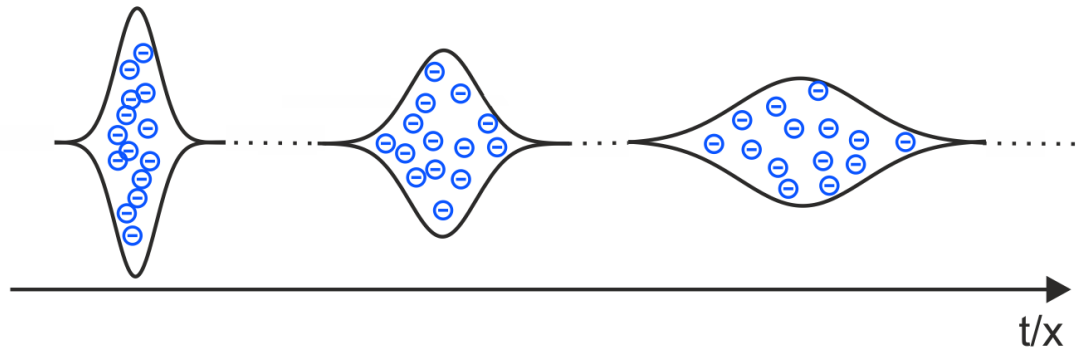

Figure 2.3: Space charge broadening of an electron pulse, du to Coulomb repulsion of the electrons.

3 Experimental setup for ultrafast point-projection microscopy

The following chapter describes the point-projection microscopy setup used in this thesis. It was developed by Melanie Müller [3] to investigate nanoscale devices and materials on ultrafast timescales in real-space. First, the general concept of a point-projection microscope is discussed. Then, the experimental realization is described, which is divided into three parts: the microscope itself, which is placed in an ultrahigh vacuum chamber, the commercial laser system that generates the ultrashort laser pulses and the optical setup between the laser system and the vacuum chamber.

3.1 General concept

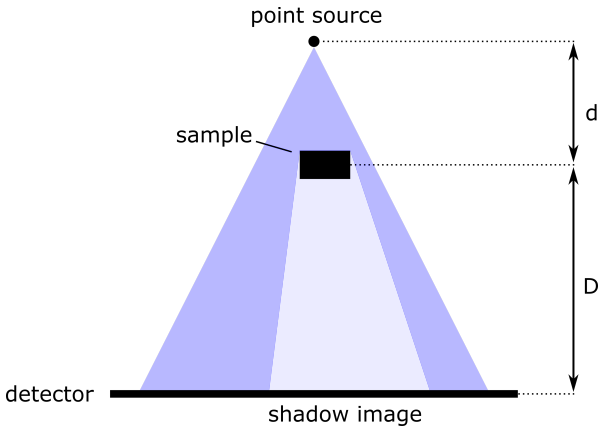

Figure 3.1: Principle of a point-projection microscope, not to scale. A point-like source illuminates a sample from a small distance d and its shadow image is detected in a large distance D. With $d \ll D$, large magnifications of the sample are achievable.

A point-projection electron microscope consists of a point-like electron source, which is placed in close proximity d to a sample [12] [13]. The created shadow image of the sample is detected in significant distance D, leading to a magnification

$$M = \frac{D}{d}, \tag{10}$$

as depicted in Figure 3.1. The electron source is realized by a laser-triggered nanotip electron emitter. Time resolution is achieved by the pump-probe technique. An ultrashort laser pulse is split into a pump and a probe excitation pulse, one of which can be

delayed with respect to the other with a delay stage. While the pump pulse excites a reversible process in the sample, the probe excitation pulse is used to trigger the nanotip electron emitter. By changing the delay between the pump and the probe excitation pulse, the reversible process can be imaged at defined points in time with femtosecond temporal resolution.

3.2 Femtosecond point-projection microscope

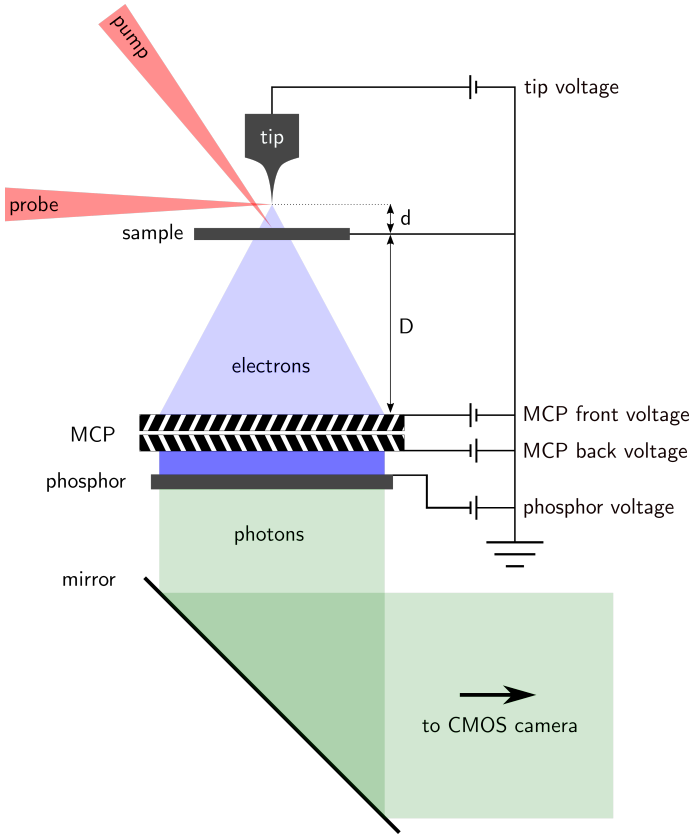

Figure 3.2: Scheme of the point-projection electron microscope. Electrons are photoemitted from a gold nanotip by a probe laser pulse. A negative voltage applied to the tip accelerates the electrons towards the sample. The resulting electron shadow image is converted into light by a combination of an MCP and phosphor screen and then captured by a CMOS camera outside the chamber. The sample can be excited by a pump laser pulse for time-resolved measurements.

All electron optics, from electron pulse generation to detection, have to be in an ultrahigh vacuum environment and thus are placed in a vacuum chamber capable of maintaining pressures down to 10^{-11} mbar. A schematic overview is depicted in Figure 3.2. The electron source is a gold nanotip, provided from the group of Markus Raschke from the

University of Boulder. It is electrochemically etched from a polycrystalline gold wire and has a tip opening angle of 12° and an apex radius of 50 nm. Figure 3.3 shows a scanning electron microscope image of the tip. The pump and probe laser beams enter the chamber through glass windows and are focused by off-axis parabolic mirrors inside the chamber. To place and align the tip apex inside the 6 µm focus of the probe excitation beam, the tip is mounted on a nanometer precision 4-axis positioning system. A negative voltage of a few hundred volts is applied to the tip. It lowers the effective work function of the tip and accelerates the photoemitted electrons towards the sample, which is mounted on a separate 6-axis positioning system, facing the tip apex. Again, nanometer precision allows for alignment in the pump laser beam as well as selection of the region of interest. For high magnification, the tip-sample distance d is usually a few microns. In this thesis however, it is several hundred microns to achieve the required field of view. The shadow image, which is created by the electrons passing the sample, is detected in a distance $D \simeq 10\,\mathrm{cm}$. A micro-channel-plate (MCP) multiplies incident electrons, which are then further accelerated onto a phosphor screen. A negative voltage can be applied to the front of the MCP to suppress low-energy secondary electrons. A Hamamatsu Orca Flash CMOS camera outside the chamber picks up the light emitted from the phosphor screen via a mirror.

For one measurement, a Keysight B2987A electrometer was connected to the tip to directly measure the current emitted by the tip. It was able to supply a voltage up to 1000 V and measure the current down to femtoamperes at the same time.

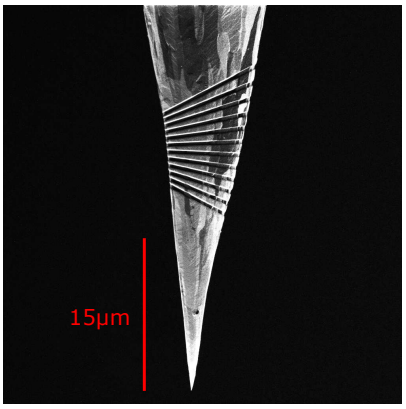

Figure 3.3: Scanning electron microscope image of a gold nanotip like the ones used in this thesis. The tips are provided by the group of Markus Raschke from Boulder University. They are produced by electrochemical etching of a polycrystalline gold wire. A grating coupler is cut into the shaft 20 µm from the apex by focused ion beam milling. It can be used for the excitation of surface plasmon ploaritons [14] [15]. In this thesis, only electron emission induced by direct laser illumination on the nanotip apex was investigated.

3.3 Laser system

The laser system is based on a Ti:Sapphire oscillator [16] (Venteon Pulse One) seeding a Yb-fiber laser amplifier and a two-stage optical parametric chirped pulse amplifier [17] (Laser Quantum venteon OPCPA) which can be operated at a repition rate of 2 MHz, 1 MHz, 500 kHz or 200 kHz. Figure 3.4 shows a schematic overview of the laser system.

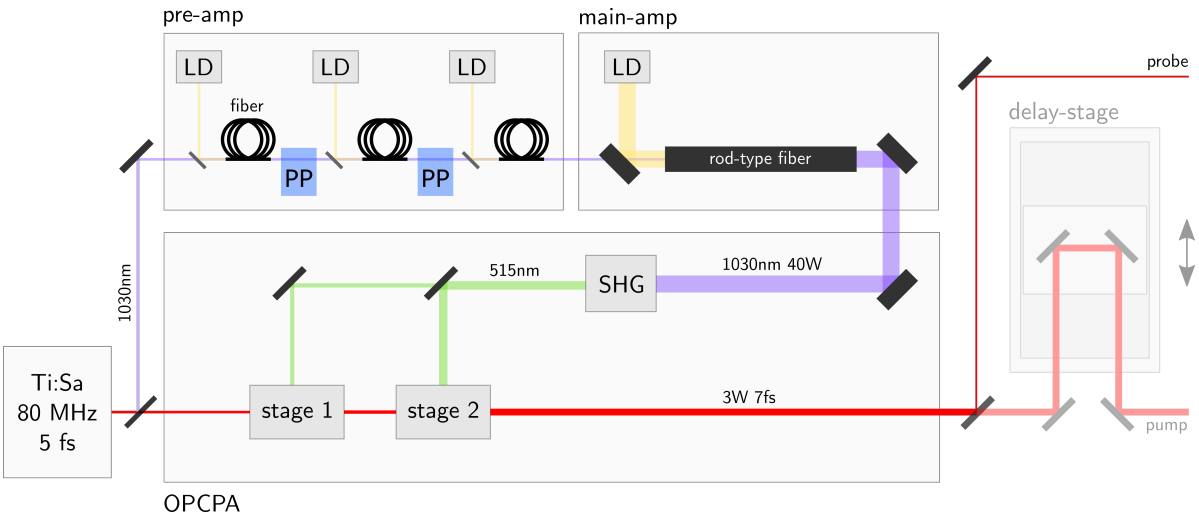

Figure 3.4: Overview of the laser system. From the output spectrum of an 80 MHz Ti:Sapphire oscillator, a narrow band around 1030 nm gets separated. It passes a laser diode (LD) pumped three stage fiber pre-amplifier and a rod-type main amplifier. Pulse pickers (PP) reduce the repetition rate to either 2 MHz, 1 MHz, 500 kHz or 200 kHz. By second harmonic generation (SHG), light with half the wavelength is produced. It pumps two optical parametric amplifier stages, that amplify the main part of the oscillator spectrum.

A Coherent Verdi pumps the Ti:Sapphire oscillator, which runs at a repetition rate of 80 MHz, and generates ultrashort laser pulses of 5 fs pulse length and 2 nJ pulse energy. Its spectrum is very broadband and ranges from about 550 nm to 1200 nm. The spectral components at 1030 nm are separated and pass a laser diode (LD) pumped fiber amplifier. Its output serves as the pump beam for the OPCPA, which then amplifies the rest of the oscillator spectrum.

The pump amplification happens in four stages: three fiber pre-amplifiers and one rod-type main-amplifier. Pulsepickers after the first and second pre-amplifier reduce the repetition rate to 2 MHz, 1 MHz, 500 kHz or 200 kHz. The laser then passes the rod-type fiber which provides most of the energy.

By second harmonic generation (SHG) in a nonlinear crystal, light with a wavelength of 515 nm is produced. It pumps a two-stage optical parametric amplifier (OPA), which amplifies the main part of the oscillator spectrum. Figure 3.5 shows the output spectrum of the laser system.

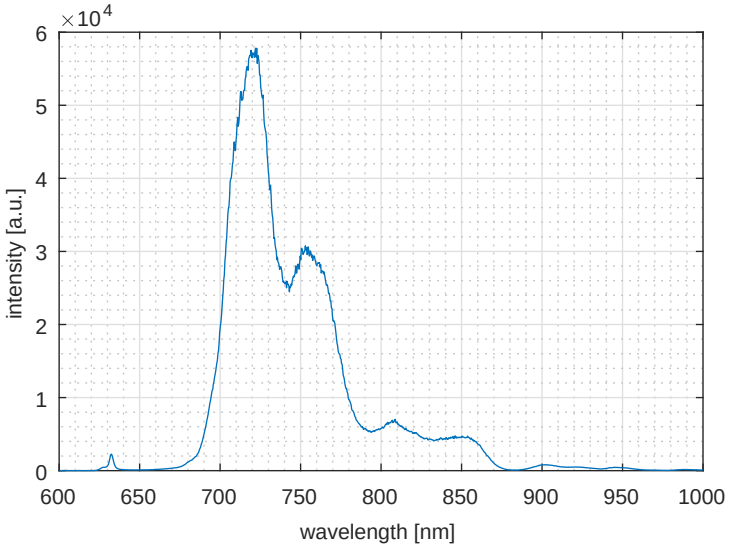

Figure 3.5: Spektrum of the output of the laser system.

3.4 Optical setup

Dispersion compensating mirrors and a pair glass wedges on linear stages were used to pre-compensate for dispersion induced by glass windows and air between the laser output and the tip.

The laser power was adjusted by a pair of continuously variable reflecting neutral density filters. One was placed on a linear stage to be adjustable. First, it was placed after the beam stabilization and the laser power was measured behind the tip, neglecting the small amount absorbed by the tip. This is shown in Figure 3.6. While in the beginning, the stage was moved manually and everything worked fine, it was later automated by a computer-controlled stepper motor, attached with rubber bands. This induced a drift of the laser focus inside the chamber. To compensate for that, the stage was placed before the beam stabilization. Then the second, static, filter was put after the beam stabilization in a slight angle to the beam so the powermeter could pick up the reflection and measure the power without passing the tip as depicted in Figure 3.7.

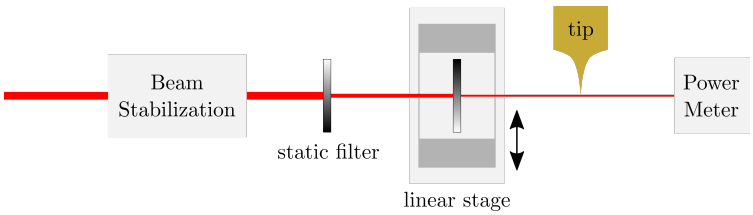

Figure 3.6: Optical setup 1. Once the stepper motor was attached to it, the variable filter induced a position dependent displacement of the laser spot, that the beam stabilization could not compensate for, because the filter was placed after it. The power-meter picked the beam after passing the tip, making it sensitive for tip positioning.

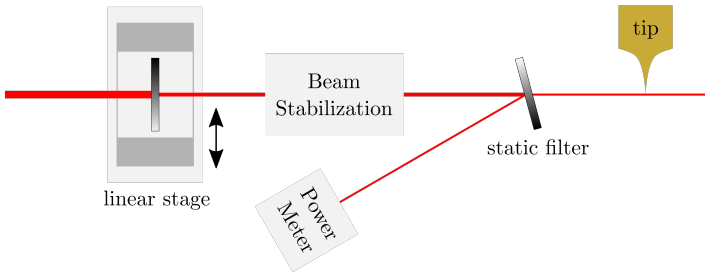

Figure 3.7: Optical setup 2. Placing the filter before the beam stabilization solved the problem. Also, the power meter picks up a reflection before the beam passes the tip, removing influence of the tip position.

For the measurement the variable filter was set to a starting position and then moved in small steps to scan the laser power. For each position, a laser power and image acquisition was performed. Data was averaged up to 10 minutes per step when the signal was low.

4 Characterization of the nanotip electron source

For the use in a point-projection microscope, the highest possible electron intensity is desired. This increases statistics and decreases measurement time. The upper limit for electron intensity is defined by several disadvantageous effects that emerge at high laser powers and electron counts: electrons emitted by optical field emission have a larger energy spread compared to multiphoton photoemission [18] and emission of more than one electron per pulse leads to space charge effects. Both impact spatial and temporal resolution of the microscope negatively and need to be avoided.

Prior to this work, the point-projection microscopy setup was operated with the Ti:Sapphire oscillator only. With its 80 MHz repetition rate, only small pulse energies could be used to avoid thermal damage of the tip. The electron source was operated in a regime far away from optical field emission, and with on average 10^{-4} emitted electrons per pulse, space charge was not an issue. The laser system was recently upgraded by the laser amplifier described in section 3.3. Now, the lower repetition rate allows for higher pulse energies and both optical field emission and space charge regimes can be reached. The aim of this thesis is to identify the optimal operation conditions of the nanotip electron source for the use in the ultrafast point-projection microscope, operated with the new laser system at repetition rates between 200 kHz and 1 MHz. In the following chapter, first, the image analysis is described. Then, the laser fluence dependency of the image intensity is investigated to make a statement about the contributing emission processes and the reduction of image sharpness due to space charge effects is discussed at different laser repetition rates. In the last section the total electron emission as measured by the electrometer is compared to the electrons reaching the detector, identified by the image intensity.

4.1 Image analysis

For the characterization of the nanotip electron source, the shadow image of an empty copper TEM grid is investigated at different laser pulse energies. The image intensity relates directly to the electron pulse intensity and the reduction of image sharpness is used as an indicator for space charge broadening. The defined edges of the TEM grid are used to determine image blurring, while the electron pulses freely passed the unobstructed holes, which is beneficial for intensity determination. Figure 4.1 shows two point-projection images, acquired at different laser pulse energies. A reduction of

image sharpness at higher pulse energy is visible. Because the images are normalized, the differences in intensity are not visible. The protrusions on the edges of the TEM grid are local accumulations of charge, deflecting the electron pulse.

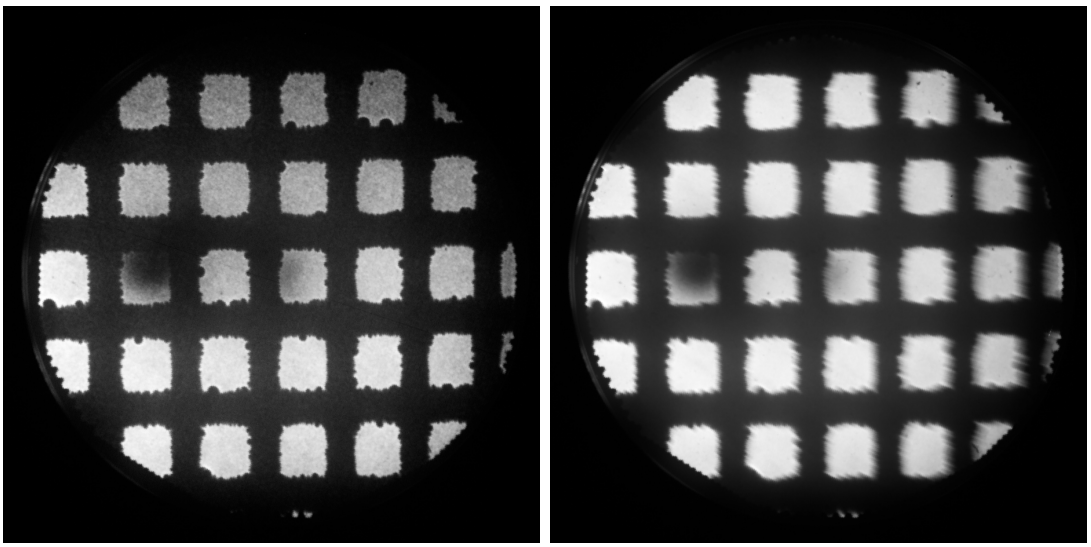

(a) 1.42 nJ pulse energy **(b)** 5.35 nJ pulse energy

Figure 4.1: Normalized point-projection images of a copper TEM grid at two different laser pulse energies. Image sharpness in image b) is reduced by space charge broadening of the electron pulses. The dark spot in the mid-left of the images originates from the structure of the MCP: The channels are tilted by an angle of 8° with respect to the normal. If electrons enter the channels in a similar angle, the gain of the MCP is reduced. Tip voltage: −150 V. MCP front voltage: −10 V.

A quantitative method for image sharpness determination is required. The intensity profile across an edge of the TEM grid contains a steeper transition from high to low intensity when the image is sharper. The error-function

$$F(x) = \frac{a}{2}\left(1 + \operatorname{erf}\left(\frac{x-\mu}{\sigma\sqrt{2}}\right)\right) + b, \tag{11}$$

with a scaling factor a, an offset b, the center μ and the standard deviation σ, is fitted to this intensity profile. The resulting sigma is used as an indicator for image sharpness and thus space charge broadening. The intensity profile was created by choosing the most homogeneous edge available and averaging all perpendicular pixel lines across it. Figure 4.2 shows edge intensity profiles at three different pulse energies, as well as the fitted error functions.

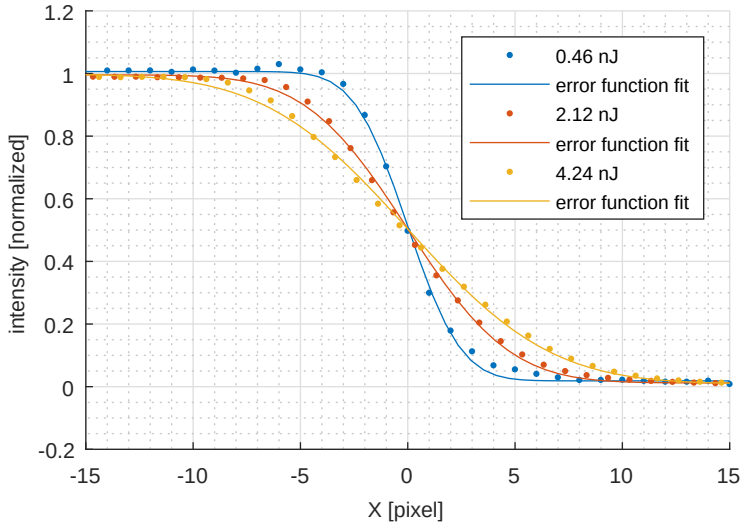

Figure 4.2: Normalized intensity profiles across an edge at different laser pulse energies with fitted error functions. A steeper transition (smaller standard deviation σ of the error function fit) relates to a sharper image.

The observed image blurring is not uniform, as Figure 4.3 shows. The blurring is more pronounced on the right side than on the left side and has a preferred, slightly radial direction. It seems like the source of the blurring lies somewhere outside the field of view. The exact shape of the blurring varied throughout the experiments, a specific correlation needs yet to be identified. A possible explanation is given in section 4.5.

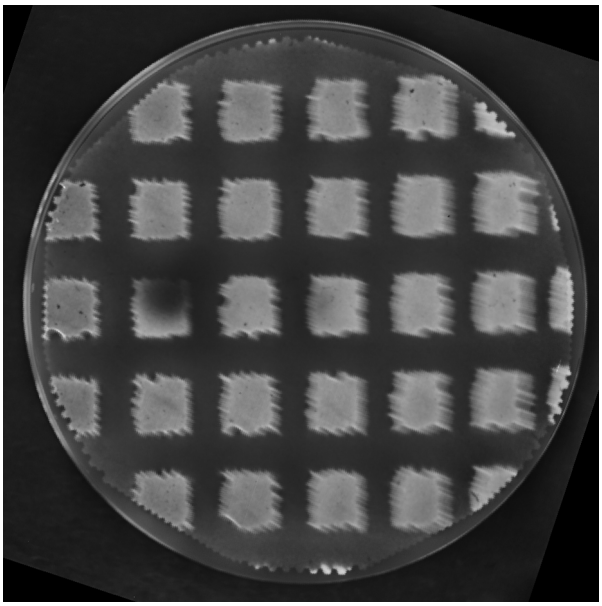

Figure 4.3: Same picture as in Figure 4.1 on the right, but with increased dynamic range to make the blurring effect more visible to the human eye. Blurring is more pronounced on the right side than on the left side and has a preferred direction.

4.2 Laser fluence dependency of photoemission

In this section, the dependence of electron emission intensity on the incident laser pulse energy is investigated. The following figures show the mean intensity of an entire image as a function of the laser pulse energy. The data is plotted on a double logarithmic scale, where a power law function results in a straight line. Its slope corresponds to the exponent, which is in this case the effective nonlinearity of the electron emission process.

In Figures 4.4 and 4.5 image intensity follows a power law up to a pulse energy of $\approx 1\,\mathrm{nJ}$. The slopes relate to a nonlinearity of 3.1 and 5.3. Above $\approx 1\,\mathrm{nJ}$, the intensity transitions into a lower order dependency of $n < 1$. The orders of ≈ 3 and ≈ 5 are indicating multiphoton photoemission: Gold has a work function of 5 eV. With the bias voltage of $-200\,\mathrm{V}$ and an assumed apex radius of 25 nm, Equations (2) and (8) give a reduction of the work function of 1.5 eV due to the Schottky effect. At least three 750 nm photons, with an energy of 1.65 eV each, are required to excite an electron from the Fermi level above the effective work function of 3.5 eV. Additionally, gold has a highly populated d-band, 2.4 eV below the Fermi level. Although more photons are required to excite these electrons, the large amount of them available could lead to a significant contribution of higher order multiphoton photoemission [19]. Hence, the measured orders are a reasonable indication for multiphoton photoemission.
The subsequent kink, which marks the transition to a low-order dependency is in the vicinity of Keldysh 1, so emerging optical field emission is a probable explanation for this behavior. This resembles data from Bormann et al. [19]. They also observed a transition from fifth order photoemission to optical field emission at a similar laser intensity.

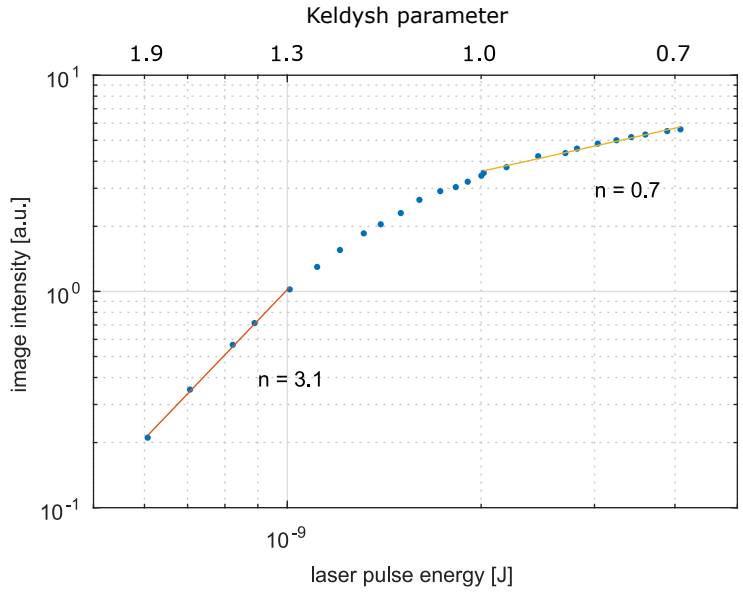

Figure 4.4: Overall image intensity as a function of laser pulse energy on a double-log scale. The corresponding Keldysh parameters are displayed on the top x-axis. Below a pulse energy of $\approx 1\,\mathrm{nJ}$, the image intensity follows a power law with $n = 3.1$. Then it kinks and follows $n = 0.7$. The transition to Keldysh < 1 indicates optical field emission (Settings: $-200\,\mathrm{V}$ tip voltage, $500\,\mathrm{kHz}$ repetition rate, optical setup 'one' – manual).

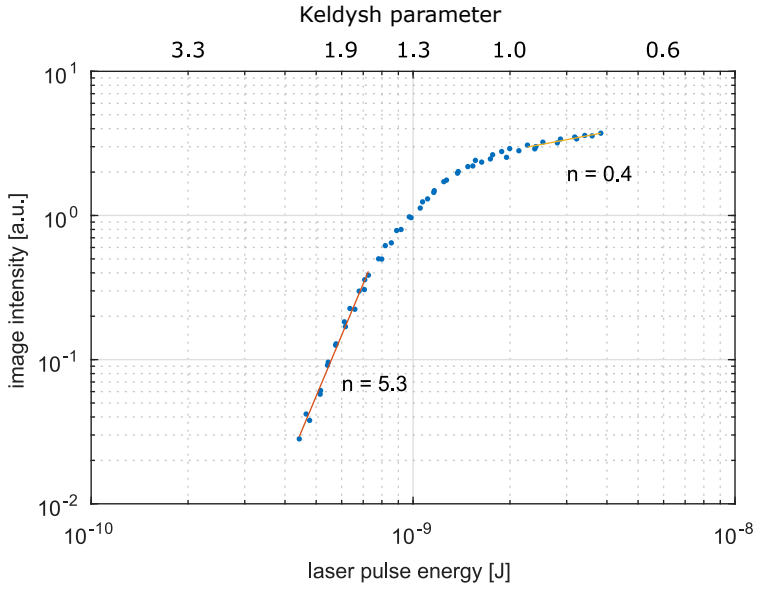

Figure 4.5: Measurement similar to the one in Figure 4.4. The nonlinearity is 5.3 at low pulse energies and 0.4 at high pulse energies(Settings: $-200\,\mathrm{V}$ tip voltage, $1\,\mathrm{MHz}$ repetition rate, optical setup 'two' – automated).

The emission process is strongly dependent on tip alignment. When the data shown in Figure 4.6 was taken, the nanotip was probably out of laser focus. In contrast to the figures described above, it does not show any transition to another emission regime. Multiphoton photoemission with an effective nonlinearity of 3.3 is dominant until the intensity suddenly drops off at highest pulse energies. At the same measured laser power the peak intensity at the apex was not high enough to enter the optical field emission regime. The sudden drop can be explained by a drift of the laser focus due to the automation of optical setup 'one' as explained in section 3.4.

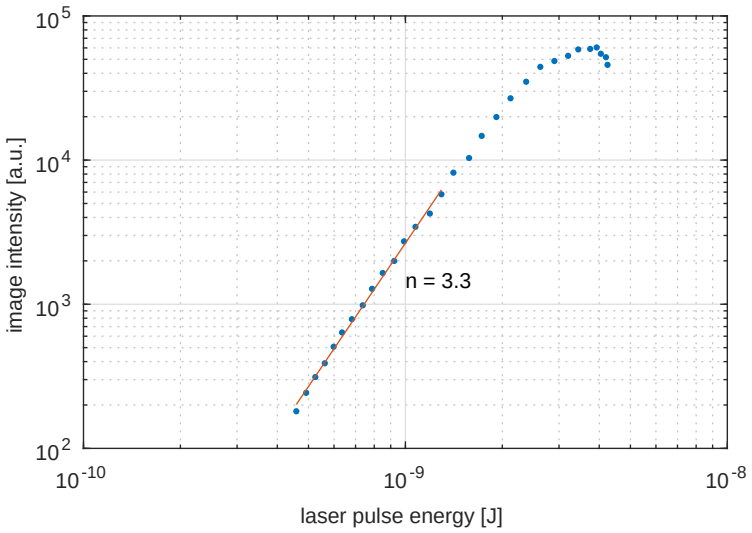

Figure 4.6: Measurement similar to the ones shown above. Photoemission with an effective nonlinearity of $n = 3.3$ is the dominating process, no transition to optical field emission is visible. Probably the tip was differently aligned than in the measurements shown before. The sudden drop at highest pulse energies originates from the problems with the automation in optical setup 'one', as explained in section 3.4. (Settings: $-200\,\mathrm{V}$ tip voltage, $1\,\mathrm{MHz}$ repetition rate, optical setup 'one' – automated)

4.3 Laser fluence dependency of image sharpness

This section discusses the influences of high laser fluences on the image sharpness. As described in Section 4.1, the edge width of an empty copper grid, represented by the standard deviation sigma of an error function, fitted to the intensity profile across that edge, is used as an indicator for image sharpness. Figure 4.7 shows sigma as a function of incident laser pulse energy. Sigma stays constant up to a pulse energy of $\approx 1\,\mathrm{nJ}$, from where it starts to increase. Most likely, this shows the transition to the emission of more than one electron per pulse, inducing space charge broadening. The drop-off at highest

pulse energies again originates from the drifting laser focus, induced by the automated optical setup 'one'.

Space charge broadening is solely dependent on the number of electrons emitted. The image intensity directly correlates with the electron intensity and thus with the number of electrons emitted. A plot against laser pulse energy is very sensitive to tip alignment and focus drift, as electron emission is a nonlinear process. Plotting against image intensity instead, overcomes these influences. In Figure 4.8, sigma is plotted directly against the image intensity from Figure 4.6, cancelling the drop-off due to reduced electron emission. The space charge broadening follows a linear dependency.

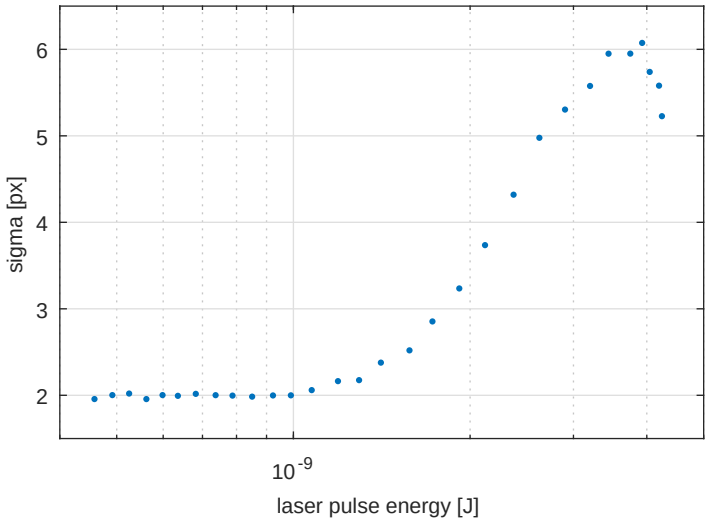

Figure 4.7: Sigma as a function of laser pulse energy. Smaller sigma means sharper image. Up to a pulse energy of 1 nJ image sharpness is constant. Above, it starts to decrease. This is caused by space charge broadening, which emerges at electron pulses containing more than one electron. Hence, the onset of image blurring shows the transition through the single-electron regime. The drop-off at highest pulse energies originates from the reduced electron emission, observed in Figure 4.6.

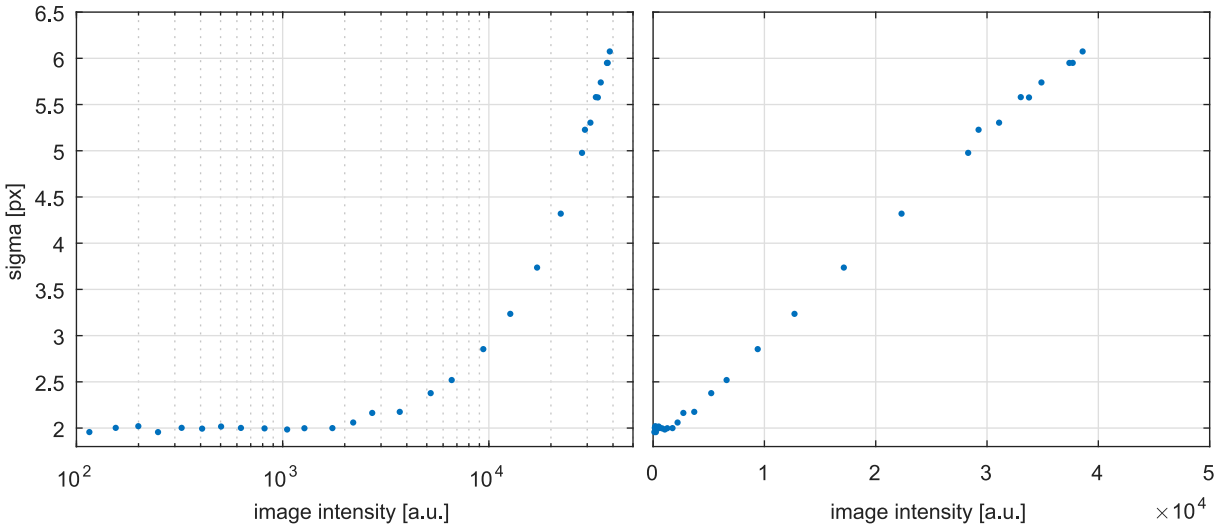

Figure 4.8: Sigma as a function of image intensity instead of pulse energy. Space charge broadening is solely dependent on the number of emitted electrons, for which image intensity is a more direct indicator. It skips the nonlinear photoemission process, which makes it insensitive to alignment and drifts, canceling the drop-off due to the reduced electron emission visible in Figure 4.7.
Left: logarithmic x-scale.
Right: linear x-scale.

4.4 Comparison between repetition rates

As space charge broadening is dependent on the number of emitted electrons per pulse, a higher laser repetition rate should increase the mean image intensity without affecting the image sharpness. Figure 4.9 compares image intensity- and image sharpness plots for 200 kHz, 500 kHz and 1 MHz, normalized to a single pulse. In theory, the graphs should overlap perfectly, but they slightly mismatch due to drifts in the setup.

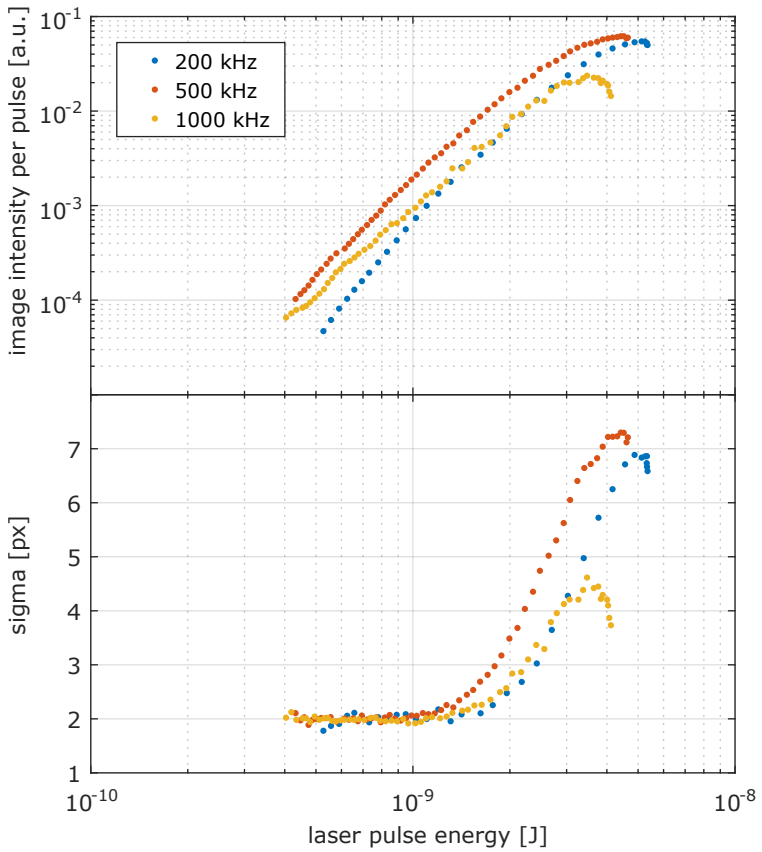

Figure 4.9: Image intensity per pulse and image sharpness versus laser pulse energy. The plots do not overlap perfectly because of drifts in the setup.

Figure 4.10 shows sigma versus the image intensity, which again circumvents the dependency on tip alignment. On the left, sigma is plotted against the image intensity per pulse and all graphs overlap, as expected. On the right it is plotted against the mean image intensity. At higher repetition rates, image sharpness reduces at a higher image intensity compared to lower repetition rates.

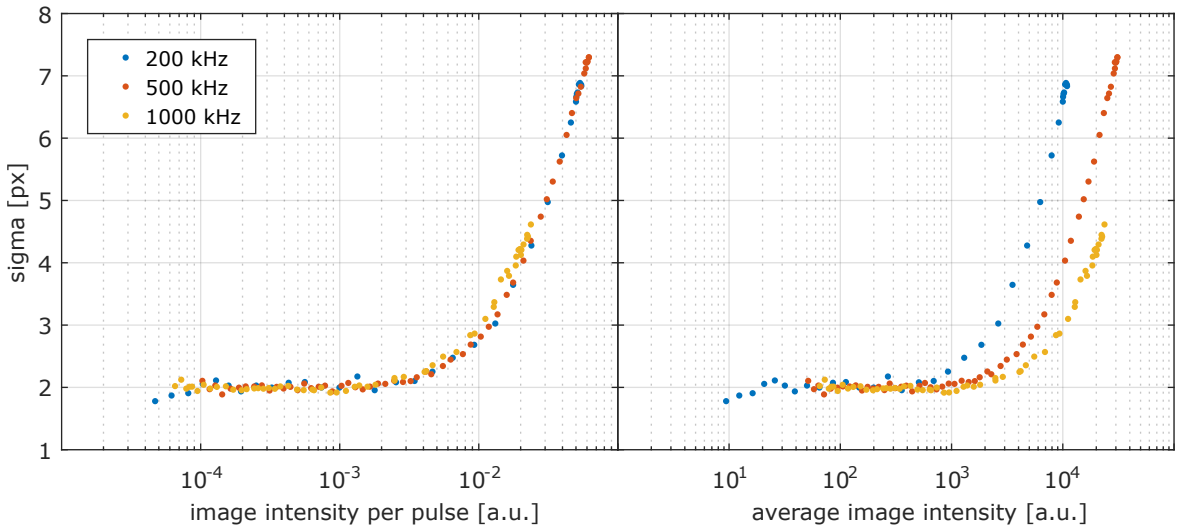

Figure 4.10: Plotting sigma against image intensity uncouples the plots from laser focus drifts.
Left: sigma versus image intensity per pulse. Because sigma is solely dependent on electrons emitted per pulse, the graphs overlap.
Right: sigma versus mean image intensity. Higher repetition rates lead to sharper images at the same intensity.

4.5 Image intensity versus tip current

To know the absolute number of electrons emitted per laser pulse, a Keysight B2987A Electrometer was used to directly measure the current flowing through the tip. The number of electrons per pulse can be derived by dividing the current by the repetition rate and the electron charge.

Figure 4.11 shows the number of emitted electrons per pulse as a function of incident laser pulse energy. The pink curve shows data from the electrometer, representing the total number of electrons emitted by the tip. The green curve is the mean image intensity (as in section 4.2), representing the fraction of the electrons that reach the detector. It is normalized to match the electrometer data at the lowest pulse energy, which does not mean that all emitted electron reach the detector. The two curves diverge with increasing pulse energy. This indicates a change in the emission profile, as proportionally more electrons are emitted outside the field of view of the detector.
Figure 4.12 shows sigma, as indicator for image sharpness and thus space charge broadening, and the ratio between total emitted electrons and the electrons that reach the detector. Clearly, both quantities are directly correlated, implying that the same effect

that causes blurring of the image is also responsible for the change of the emission profile. This can be explained by two possible scenarios:

Either, the sharpness reduction is caused by space charge broadening of electrons emitted close to the center of the apex, i.e., from electrons that reach the detector. In this case, their repulsion must be so strong, that the emission cone is significantly widened, causing a change of the emission profile that correlates with the image blurring. This is less likely to be the case, as very large changes of the emission angle would be required. Bormann et al. [19] did not observe any widening of the emission cone at similar electron counts per pulse.

Alternatively, increasing the laser pulse energy might lead to enhanced emission of electrons from outer areas of the apex, i.e. electrons that do not reach the detector. They, however, deflect the electrons emitted from the apex center that do reach the detector, inducing the observed space charge blurring. This is more likely to be the case, as it would explain the preferred direction of image blurring, shown in Figure 4.3. As observed by Müller [3], intense emission of electrons can occur from the shadow side of the apex which do not reach the detector without focusing of the electron beam. While this could explain the blurring-character in some images, it is still unclear if this can also explain the different patterns observed during the experiments.

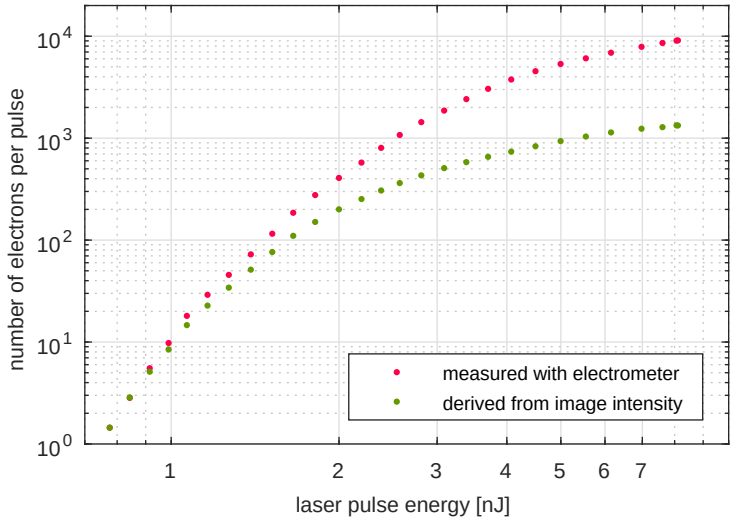

Figure 4.11: Number of electrons emitted per pulse versus the incident laser pulse energy. Pink shows data obtained by a electrometer directly measuring the tip current. Green was derived from the image intensity and normalized to match pink at the lowest pulse energy. The increasing deviation between both curves shows a change of the emission profile, as relatively more electrons are emitted, that do not reach the detector.

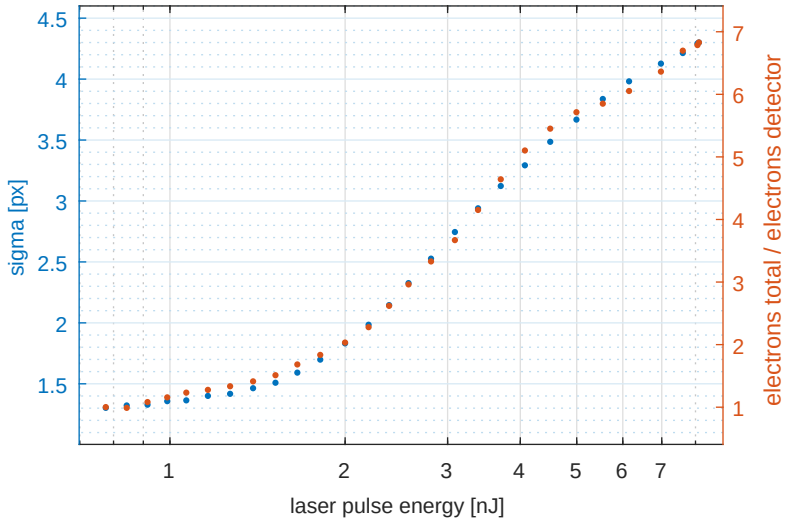

Figure 4.12: Sigma, as an indicator for image sharpness (left y-axis) and the ratio between the total number of electrons emitted and the electrons reaching the detector (right y-axis). They show a strong correlation.

5 Summary and outlook

In this thesis, photoemission from a nanotip electron source is investigated, focusing on optimal performance inside a femtosecond point-projection microscope. The usage of a 0.2 to 2 MHz laser system allows for exceeding the single electron regime, which makes space charge broadening of the electron pulses a considerable effect. To characterize the regime of highest usable current while operating in the single electron limit, the image intensity and image sharpness of the point-projection images are analyzed. Changes in the power dependence show a transition from multiphoton photoemission to optical field emission and the image sharpness decreases as the multi-electron pulse regime is entered. Increasing the repetition rate allows for higher currents without space charge induced blurring. The additional direct measurement of the tip current shows an increasing deviation between the total number of electrons emitted and the number of electrons reaching the detector. Increasing electron emission from the side of the apex is suspected to cause both, this deviation and the space charge blurring visible in the fsPPM images. This could be confirmed by experiments with a shorter tip-detector distance, to achieve a larger field of view.
The tips used in this work are equipped with a grating coupler, 20 µm from the tip apex (Figure 3.3), for the excitation of surface plasmon polaritons [14]. It can be used to remotely trigger electron emission without direct apex illumination. It is of high interest if this could suppress the supposed emission of electrons from the edge of the apex. If so, the fraction of electrons reaching the detector would be larger, leading to much higher image intensities before entering the space charge regime.

While this work showed how space charge affects the spatial resolution of a fsPPM, the effects on temporal resolution were not investigated. In a follow-up experiment, our group performed pump-probe measurements of ultrafast photoemission from silver nanowires at different tip currents. As tip electron emission entered the multi-electron regime, the measured duration of the ultrafast process increased, indicating a reduction of the temporal resolution due to space charge broadening.

6 References

[1] M. Gulde, S. Schweda, G. Storeck, M. Maiti, H. K. Yu, A. M. Wodtke, S. Schafer, and C. Ropers, "Ultrafast low-energy electron diffraction in transmission resolves polymer/graphene superstructure dynamics," *Science*, vol. 345, pp. 200–204, jul 2014.

[2] L. Waldecker, R. Bertoni, and R. Ernstorfer, "Compact femtosecond electron diffractometer with 100 keV electron bunches approaching the single-electron pulse duration limit," *Journal of Applied Physics*, vol. 117, no. 4, 2015.

[3] M. Müller, *Femtosecond low-energy electron imaging and diffraction using nanotip photoemitters*. dissertation, Freie Universität Berlin, 2016.

[4] M. Müller, A. Paarmann, and R. Ernstorfer, "Femtosecond electrons probing currents and atomic structure in nanomaterials," *Nature Communications*, vol. 5, p. 5292, oct 2014.

[5] H. B. Michaelson, "The work function of the elements and its periodicity," *Journal of Applied Physics*, vol. 48, no. 11, pp. 4729–4733, 1977.

[6] P. Hommelhoff, Y. Sortais, A. Aghajani-Talesh, and M. A. Kasevich, "Field emission tip as a nanometer source of free electron femtosecond pulses," *Physical Review Letters*, vol. 96, no. 7, pp. 1–4, 2006.

[7] M. Krüger, M. Schenk, P. Hommelhoff, and M. Kruger, "Attosecond control of electrons emitted from a nanoscale metal tip.," *Nature*, vol. 475, no. 7354, pp. 78–81, 2011.

[8] L. V. Keldysh, "Ionization in the field of a strong electromagnetic wave," *Soviet Physics JETP*, vol. 20, no. 5, pp. 1307–1314, 1965.

[9] R. Gomer, "Field emission, field ionization, and field desorption," *Surface Science*, vol. 299-300, no. C, pp. 129–152, 1994.

[10] A. Paarmann, M. Gulde, M. Müller, S. Schäfer, S. Schweda, M. Maiti, C. Xu, T. Hohage, F. Schenk, C. Ropers, and R. Ernstorfer, "Coherent femtosecond low-energy single-electron pulses for time-resolved diffraction and imaging: A numerical study," *Journal of Applied Physics*, vol. 112, p. 113109, dec 2012.

[11] B. J. Siwick, J. R. Dwyer, R. E. Jordan, and R. J. D. Miller, "Ultrafast electron optics: Propagation dynamics of femtosecond electron packets," *Journal of Applied Physics*, vol. 92, no. 3, pp. 1643–1648, 2002.

[12] E. Quinonez, J. Handali, and B. Barwick, "Femtosecond photoelectron point projection microscope," *Review of Scientific Instruments*, vol. 84, no. 10, 2013.

[13] A. R. Bainbridge, C. W. Barlow Myers, and W. A. Bryan, "Femtosecond few-to single-electron point-projection microscopy for nanoscale dynamic imaging," *Structural Dynamics*, vol. 3, p. 023612, mar 2016.

[14] M. Müller, V. Kravtsov, A. Paarmann, M. B. Raschke, and R. Ernstorfer, "Nanofocused Plasmon-Driven Sub-10 fs Electron Point Source," *ACS Photonics*, vol. 3, no. 4, pp. 611–619, 2016.

[15] J. Vogelsang, J. Robin, B. J. Nagy, P. Dombi, D. Rosenkranz, M. Schiek, P. Groß, and C. Lienau, "Ultrafast Electron Emission from a Sharp Metal Nanotaper Driven by Adiabatic Nanofocusing of Surface Plasmons," *Nano Letters*, vol. 15, pp. 4685–4691, jul 2015.

[16] S. Rausch, T. Binhammer, A. Harth, E. Schulz, M. Siegel, and U. Morgner, "Few-cycle oscillator pulse train with constant carrier-envelope- phase and 65 as jitter," *Optics Express*, vol. 17, no. 22, pp. 20282–20290, 2009.

[17] M. Schultze, T. Binhammer, G. Palmer, M. Emons, T. Lang, and U. Morgner, "Multi-μJ, CEP-stabilized, two-cycle pulses from an OPCPA system with up to 500 kHz repetition rate.," *Optics Express*, vol. 18, no. 26, pp. 27291–27297, 2010.

[18] M. R. Bionta, S. J. Weber, I. Blum, J. Mauchain, B. Chatel, and B. Chalopin, "Wavelength and shape dependent strong-field photoemission from silver nanotips," *New Journal of Physics*, vol. 18, p. 103010, oct 2016.

[19] R. Bormann, M. Gulde, A. Weismann, S. V. Yalunin, and C. Ropers, "Tip-enhanced strong-field photoemission," *Physical Review Letters*, vol. 105, no. 14, pp. 1–4, 2010.

Freie Universität Berlin

Selbstständigkeitserklärung

Name:	(Nur Block- oder Maschinenschrift verwenden.)
Vorname:	
geb.am:	
Matr.Nr.:	

Ich erkläre gegenüber der Freien Universität Berlin, dass ich die vorliegende _____ selbstständig und ohne Benutzung anderer als der angegebenen Quellen und Hilfsmittel angefertigt habe.

Die vorliegende Arbeit ist frei von Plagiaten. Alle Ausführungen, die wörtlich oder inhaltlich aus anderen Schriften entnommen sind, habe ich als solche kenntlich gemacht.

Diese Arbeit wurde in gleicher oder ähnlicher Form noch bei keiner anderen Universität als Prüfungsleistung eingereicht und ist auch noch nicht veröffentlicht.

Datum: _____ Unterschrift: _____

(_____)